Novel Applications of State-of-the-Art Gamma-Ray Imaging Technique: From Nuclear Decommissioning and Radioprotection to Radiological Characterization and Safeguards

Filippo Gagliardi[ID], Luigi Lepore[ID], Luigi Meschini, Alessandro Ciotoli[ID], Nadia Cherubini, Luca Falconi, Davide Formenton, Giada Gandolfo[ID], Edoardo Gorello, Giuseppe A. Marzo[ID], Egidio Mauro, Marco Pagliuca, and Andrea Roberti

Abstract—Gamma-ray imaging is a powerful technique subjected to important research efforts in nonmedical fields, providing information about the possible spatial distribution of radioactive materials emitting photons and potential contamination spots, in generic area survey or to specific component analyses. This capability opens up a range of possible applications in nuclear installations and radioactive waste management sites, where radiation survey protocols and radiological characterization of items may be highly and positively impacted by this technique. In this work, a new-generation 3-D pixelated CdZnTe gamma-ray imaging and spectrometry detector has been used in the context of the TRIGA RC-1 Research Reactor at the ENEA Casaccia Research Centre to test several applications where gamma-ray imaging can provide valuable information otherwise unknown (with equivalent level of accuracy and effort). Experiments carried out range from radiological survey, where hotspots are identified and radioactive items are sorted from conventional waste to improvements in the quantification of gamma emitters via gamma-spectrometry analysis, and from safeguards and nonproliferation purposes (e.g., providing methods to assess the amount of special nuclear material (SNM), which remains fixed and unchanged in time) up to radiation protection issues (e.g., identification of unexpected contributions to personnel total exposure). The results obtained in this experimental campaign, as well as the validations provided by comparison with "traditional" methods, demonstrate the applicability of state-of-the-art gamma-ray imaging systems to the presented tasks, with consequences that could positively impact the current radiation survey routines and radiological characterization protocols followed at ENEA TRIGA RC-1 as well as other installations.

Index Terms—Gamma-ray imaging, nuclear decommissioning, quantitative gamma spectrometry, radiation protection, radioactive waste management, radiological survey, safeguards and nonproliferation, TRIGA research reactor.

I. INTRODUCTION

IMAGING with gamma rays is a powerful technique widely used in nuclear medicine therapy and diagnosis [1], [2], [3], being able to provide visual information about the distribution of body-injected radioactive elements emitting photons, improving knowledge of the patient status to optimize medical care. The application in nonmedical fields, e.g., in the industrial nuclear field (e.g., power plants, research reactors, nuclear fuel fabrication and reprocessing installations, research laboratories, and waste management sites), is the natural step to be walked in the development of such technique. Obviously, the industrial nuclear field presents many differences with respect to classic nuclear medicine applications. The main differences are the variability and complexity of the environment and objects to be analyzed (both in situ and in laboratories), the wide range of radionuclides in the radiological inventory, and the amount of radioactivity often unknown before the investigation.

The world of gamma imaging systems applicable to the nuclear field has rapidly grown in the last decades thanks to the improvements achieved in crystal manufacturing, electronics, and algorithms. Different systems exist on the market (or as prototypes) with different characteristics [4], [5], [6], [7], [8], [9], [10], [11], [12]. Despite each single system performance, their true application range is still unclear, making gamma-ray imaging still a "niche" technique in the industrial nuclear field.

Nucleco SpA, the main company in Italy performing decommissioning on nuclear installations, radiological characterization, and radioactive waste management, has tested and

Fig. 1. (a) NGI system in action while measuring a pipe and (b) tank in a BWR reactor.

Fig. 2. Background-free NGI gamma-ray spectra with mixed radionuclides. The ^{137}Cs energy resolution was measured at 0.83% FWHM.

used a state-of-the-art gamma-ray imaging system for several applications in the last years, trying to understand and qualify its full potential [13], [14], especially for (although not limited to) facility decommissioning actions. Recently, the interest of application was raised also in reactor facility management, and thus, an experimental campaign has been performed at the TRIGA RC-1 Research Reactor at the ENEA Casaccia site, Rome.

In particular, in [14], preliminary results regarding the application of this technique to the real case of a TRIGA reactor to assess its capabilities in a variety of tasks were presented. In this work, measurement system performances have been quantified and better investigated with the main goal to acknowledge this innovative methodology as comparable with the industrial standard applied in the field (e.g., HPGe detectors), with all the added value that "visualization" of radioactivity by human eye could produce.

II. Materials and Methods

Two Nucleco Gamma Imager (NGI, Fig. 1) systems equipped with H3D Inc. H420 systems [4], [5] based on a 3-D position-sensitive CdZnTe gamma-ray imager and spectrometer were used for acquisition and analysis at room temperature. The detector active volume consists of approximately 20 cm^3 of CdZnTe crystal with better than 1% full-width-at-half-maximum (FWHM) energy resolution at 662 keV (see Fig. 2). The crystal read-out electronics comprehend a pixelized anode coupled with a planar cathode. Utilizing the drift-time information and the induced signal collected by the pixels, this crystal geometry allows for 3-D position information (X and Y for pixel and depth, respectively) about the energy released (or deposited in the crystal) per each photon interaction. This helps guarantee such energy resolution despite the relatively high-volume crystal (the typical active volume for commercial CZT is 1 cm^3 with an energy resolution of 1.5%–2% FWHM at 662 keV).

Two different algorithms are used for imaging. Compton imaging [15], [16] is used for photon energies from 250 to 3000 keV, with an angular resolution of ≈20° FWHM on the entire solid angle. Interactions due to Compton scattering and photoelectric absorption are detected and distinguished within the crystal (provided that they happen in different pixels), as well as the energy deposited in each pixel (the total energy is assumed to be equal to the energy of the incoming photon). These data are used for calculating the scattering angle, but, for symmetry reasons, only a cone can be associated with each event r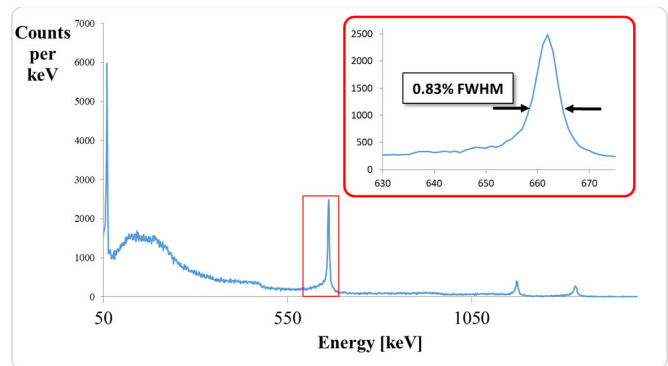ecorded: the cones generated by different events sum up in the region where effectively photons are coming from, generating the image.

Coded aperture imaging (CAI) [17], [18] is used for photon energy from 50 to 350 keV (although it can be used up to 1500 keV or higher, with lower efficiency—an examples in Section III-D), with an angular resolution of ≈5° FWHM in the mask field of view. For this energy range, photons will undergo direct photoelectric absorption, meaning that in general, the signal is read by one pixel only. The possible directions are then identified by using a 1.5-mm-thick rank-19 MURA mask made of tungsten [19].

For both algorithms, the angular precision is ±1°. The radiation field-of-view using Compton imaging is 4π (360°), while for CAI, it is limited to 86° × 86° because of the mask. This limited field-of-view is represented as a red square on the image. The imaging reconstruction is superimposed to an optical image acquired by the system: the optical image is natively a fisheye type and is corrected for parallax. The optical image frames almost entirely the frontal half of the solid angle, while the remaining part of the solid angle is represented as completely black. The Compton imaging (with its 4π field-of-view) can thus return reconstruction in the black area of optical image, which can correspond to lateral directions, backward directions, and upward/downward directions (some examples will be provided in this work).

Parallax between the camera and imaging reference frames, when viewing the optical image in the imaging reference frame, is corrected through geometry and lens intrinsics. The optical image pixel positions are converted to pixel spherical directions through the azimuthal equidistance projection [20] and optimized lens intrinsics. The optical image spherical directions are converted to Cartesian positions assuming a distance to a sphere as determined by the user or by the laser rangefinder NGI systems that are equipped with. The optical image Cartesian positions are then translated to the detector frame of reference and then converted back to spherical coordinates.

Imaging reconstruction is to be intended as a probability distribution function (where the value = 1 is like "certain"): as a direction has a color tending to red, the probability that from that direction is coming to a portion of the detected photons approaches to 1. Nevertheless, a certain statistics is needed

to ensure that the imaging is "well representing" the real radioactive distribution: the number of events needed depends upon the spread of the distribution (against the distance) and upon the signal over background (S/B) ratio: if the distribution gets larger or closer, or the S/B ratio gets smaller, the statistics needed is higher and vice versa. Moreover, the reconstruction is 2-D and computed assuming that the emission is placed at a fixed distance; thus, no effect due to varying distance (within the same radioactive distribution) and the absorption due to materials passed through is taken into account: these two effects can significantly affect the reconstruction reliability. At the end of the day, evaluating the uncertainty of the reconstruction would be meaningless if many other factors were not deeply considered. To work out a way to understand the reliability of the distribution, the system's software is equipped with an experimental gauge based upon the S/B ratio, which evaluated if the number of events was enough to determine a "good" imaging reconstruction.

Besides the imaging reconstruction, another kind of analysis can be performed. The time spectrum, i.e., the counts per second (cps) of all gamma rays or only for a desired energy range versus time, can be analyzed to evaluate the temporal evolution of any signal of interest, which could be influenced in case radiological status changes.

NGI gamma-ray spectra were analyzed for quantitative determination of detected radionuclide activity (and minimum detectable activity (MDA) for all the radionuclides of interest) by using the SourceTerm tool in the Visualizer software by H3D Inc., including a special feature under development with Nucleco support [21]. For each measurement configuration, SourceTerm estimates the total detection efficiency for required energies, obtained by multiplying the measured detector efficiency in air by a correction due to absorption in materials passed through and distance based upon a point-kernel-based calculation [22]. Photopeak count rates are then converted to absolute activities, with a reliability close to the industrial worldwide accepted standard of high-purity germanium (HPGe) crystals, e.g., MIRION Technologies In Situ Object Counting Systems (ISOCS) [23].

The detector efficiency in air is measured by the producer (and verified periodically) using certified sources placed in different positions in front of the detector (over a 90° × 90° window) and averaging the results; the variation of efficiency in lateral and backward directions is not taken into account at the moment. The point-kernel-based algorithm is used to compute the distance and matrix correction: the space is imaginarily divided in elementary cells (the "point kernels"), and for each cell containing radioactivity, the correction is computed being known the path a photon has to travel to reach the detector and the materials crossed. The efficiency is averaged over the kernels, whose size is then halved (i.e., the number of cells is doubled) and the efficiency is recalculated and compared to the previous one. This loop is repeated until a desired convergence is obtained.

In this work, an ISOCS system equipped with an HPGe Canberra GX2020 detector (30% relative efficiency, energy range: 45–2000 keV, with a 5-cm-thick lead 90° collimator) has been used as a reference to compare isotope activity results

TABLE I
TRIGA RC-1 EXPERIMENTAL CHANNELS

Experimental channels	Main task/experiments performed
Thermal column	Validation of novel detectors
Tangential piercing	Neutron radiography and tomography
Radial	Neutron diffraction. Channels A, B, C actually in refurbishment
Lazy Susan	NAA, space applications, food traceability
Central Thimble	Precursor radionuclides production for radiopharmaceuticals, NAA, space applications, food traceability
Rabbit	NAA

from the NGIs. The system is equipped with the Geometry Composer software [24] that provides the total detection efficiency for each specific measurement configuration modeled using a point-kernel-based calculation.

The measurements were conducted at the TRIGA RC-1 Research Reactor at the ENEA Casaccia Research Centre (Rome). The ENEA TRIGA RC-1 is a MARK II [25], [26], thermal neutron spectrum, pool-type, water-cooled Research Reactor, originally having a thermal power of 100 kW when built in 1960, increased to 1 MW based on an in-house developed ENEA design in 1967.

TRIGA RC-1 utilization has covered in the past and covers currently a wide range of fields [25]:

1) neutron activation analysis (NAA);
2) neutron imaging;
3) forensic studies and food traceability;
4) material studies via neutron scattering and diffractometry;
5) stress test for materials and electronic components for space applications;
6) radionuclide production, e.g., for industrial applications or precursor of radiopharmaceuticals such as of ^{99m}Tc, ^{177}Lu, and ^{161}Tb;
7) detector testing; and
8) education and training.

Many experimental channels are available, and several experiments can be performed in each channel (see Table I). All the activities listed before involve the irradiation of samples, container capsules, and both supports and metal parts of the reactor and experimental setup. Neutron activation is carefully evaluated case by case during the design phase of the experiment (to understand feasibility) and verified during and after the experiment by direct measurements. Moreover, neutron activation of fluids (liquids and air mainly) and dust could produce further contributions to personnel exposure, external irradiation, and contamination.

The rationale in this work is that in the normal operation phases of the ENEA TRIGA RC-1 reactor, more than half of the day is a stand-by time (from 4:00 P.M. till 8:00 A.M. of the day after, usually) that could be used to set gamma imaging inspections to acquire longer acquisitions to deepen the radiological status of the facility.

As the first step in this work, measurements were conducted in areas where more relevant radioactivity was expected. The evaluation of "relevance" was made based upon functional reasons and periodical radiometric surveys of all the areas and main components held by the TRIGA Health Physics team. For example, at the "Reactor Top" level of the reactor, there are components used for moving the fuel elements that could be contaminated in case of a material release (thus, functional reason). Other examples are in the reactor building basement, where there is the ion-exchange resin container (both functional and radiometric reasons) and the "bunker" containing the most active sources and components (radiometric reasons).

Some preliminary acquisitions were taken to collect general information about the level of environmental background and radiological conditions, allowing for proper planning of the following detailed measurements. Then, based on the information obtained from these preliminary investigations, the focus shifted to individual components and more confined areas, physically bringing the detector closer to the objects suspected/detected to actually be radioactive.

Moreover, even areas and components with less relevant radioactivity levels have been investigated, by increasing the counting statistics, e.g., using the night time and weekend time also. This approach aimed to optimize the time for each measurement, thus dedicating longer times to less "active" areas, and to locate the radioactivity more precisely within the image frame.

III. APPLICATIONS AND RESULTS

NGIs were used at the ENEA TRIGA RC-1 Research Reactor for an experimental campaign from January 2023 to October 2023. More than 90 spectral acquisitions were carried out, with acquisition time ranging from a few minutes up to three days depending on the level of occurring radioactivity, the target imaging sensitivity, and the desired MDA. Many measurements were acquired overnight; sometimes, the detector was left in acquisition even over an entire weekend, to test its stability and look for eventual very weak signals.

The "short" measurements (few minutes long) were used only for hotspot identification, to better position the detector for longer lasting measurements. In general, the measured count rates were quite low: the maximum detected value was ≈10 cps for each ^{60}Co emission in an activated component placed in the "bunker" (≈10% of dead-time, discusser later and in [14]) and ≈50 cps for the 185.7-keV emission from ^{235}U (≈2% dead-time) for the measurement of a fuel element (discussed later). Despite the greater count rate in the ^{235}U measurement, the ^{60}Co measurement has a higher dead-time. This is due to the presence of other radioactive sources in the ^{60}Co assay, and the number of events photons from ^{60}Co must undergo before being completely absorbed (photons from ^{235}U undergo only photoelectric absorption, while photons from ^{60}Co undergo pair production and/or Compton scattering before being absorbed).

The main driver followed regarding NGIs sensitivity was not an MDA to reach, but the quality of imaging reconstruction, which depends upon the statistics collected for the desired energy range and the signal/background ratio. Furthermore,

not all the events can be used for imaging [4]: this implies that once a clear image is obtained, the associated peak on the spectrum is well distinguishable from background and, as such, the quantitative MDA is lower than the radionuclide activity.

Measurements covered the "Reactor Top" and related equipment, several views of the reactor hall ground floor, some views of the pump room in the basement, direct measurements of a fresh fuel element at the fresh fuel storage room, and radioactive waste.

According to the experience achieved during the whole campaign, with some results already presented in [14], at least five main applications have been demonstrated to be accomplished by means of modern gamma imaging systems.

1) To survey potentially contaminated areas, with identification and sorting of radioactive items.
2) To make quantitative gamma-spectrometry analysis, using NGIs is parallel or in support of the HPGe ISOCS system.
3) To provide methods to help guarantee continuity of knowledge (CoK) and prevention of diversion for nuclear safeguards and nonproliferation scopes.
4) To identify and localize known and unknown radioactive sources.
5) To provide additional radiation protection information about unexpected irradiation contributions to personnel.

These applications will be addressed in detail in the following discussion, exploiting some experimental cases.

A. Case 1: Survey of a Cabinet Content

During the survey campaign of the Reactor Top, unexpected signals of ^{60}Co (1173- and 1332-keV photon energy peaks) and ^{238}U (766- and 1001-keV photon energy peaks) coming from a cabinet containing many items (often with unknown origin) were identified [14], arising the hypothesis that special nuclear materials (SNMs) and activated items were present (see Fig. 3).

The tail in Fig. 3(b) is not due to poor statistics: the measurement taken in the opposite direction with respect to the cabinet (see Fig. 4) shows the presence of ^{60}Co-contaminated water in a small tank placed behind the detector, although a spot corresponding to the contribution of the left part of the cabinet is still present (in the dark region, corresponding to the backward direction).

Afterward, the material in the cabinet was removed and sorted according to fast radiometric evaluations, labels, and functional information, producing four small bags (two with technological waste and two with metallic items discussed further in this article) that were measured individually. The empty cabinet was measured again, confirming that all ^{60}Co content was removed, while ^{238}U was still detected. Other images have been acquired from different points of view with respect to the cabinet, trying to triangulate ^{238}U signals, which turned out to come from the fresh fuel storage room placed at a lower level of the reactor building with respect to the reactor top floor, approximately 10 m away from the detector and behind the reactor building wall (see Fig. 5).
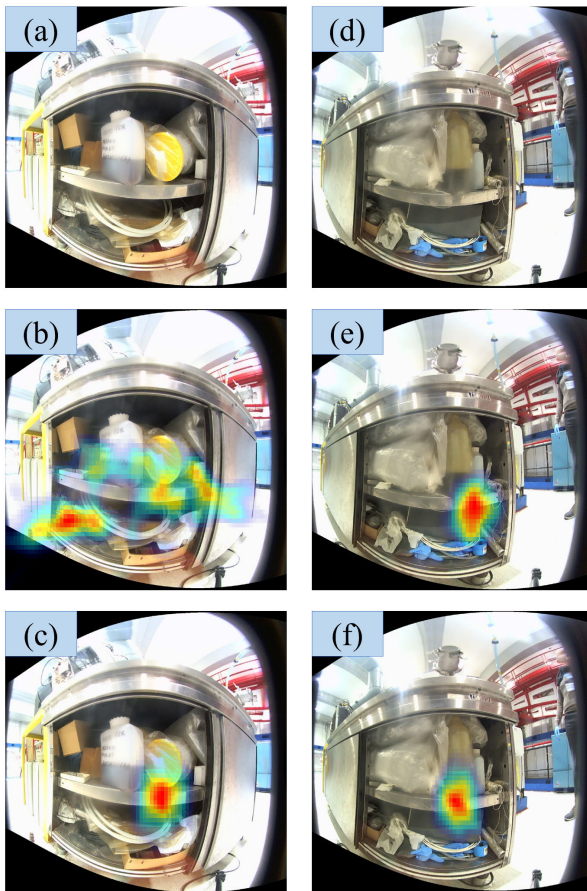
Fig. 3.   Survey of the cabinet [14]. The real time was ≈5 h for all measurements. Cabinet, left part: (a) optical image, (b) ^{60}Co (1173 and 1332 keV), and (c) ^{238}U (766 and 1001 keV). Cabinet, right part: (d) optical image, (e) ^{60}Co (1173 and 1332 keV), and (f) ^{238}U (766 and 1001 keV).
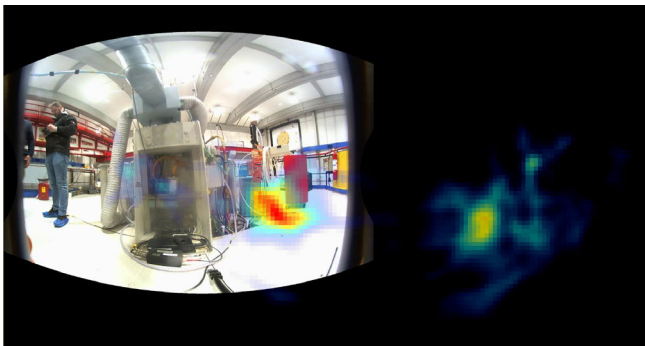

Fig. 4.   Distribution of ^{60}Co obtained pointing the detector in the opposite direction with respect to Fig. 3. The spot in the dark region on the right corresponds to ^{60}Co reconstructed on the left part of the cabinet [14].

Due to the signal attenuation of the wall, the gamma streaming contribution from the spare rods present at the fresh fuel storage room was not supposed to reach the reactor building area; yet, a stable rate of (0.044 ± 0.001) cps was detected and allowed confirmation and triangulation of the ^{238}U signal. This is now leading to further radiation protection analysis to optimize the exposure of personnel since the fresh fuel storage room is just under the reactor control room and the gangway to the reactor top floor.

Coming back to the bags created from emptying the cabinet, for the two with technological waste (plastics, paper materials,
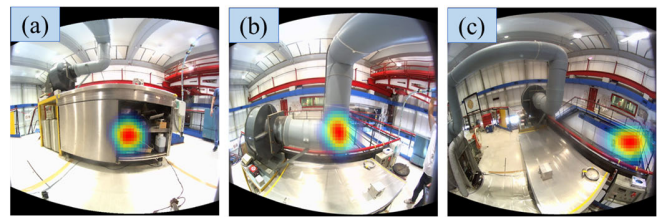

Fig. 5. ^{238}U imaged using the Compton algorithm when measuring at (a) front of the empty cabinet, (b) from top of the empty cabinet in frontal view, and (c) from the top of the empty cabinet in lateral view. The real time was ≈24, ≈19, and ≈95 h.
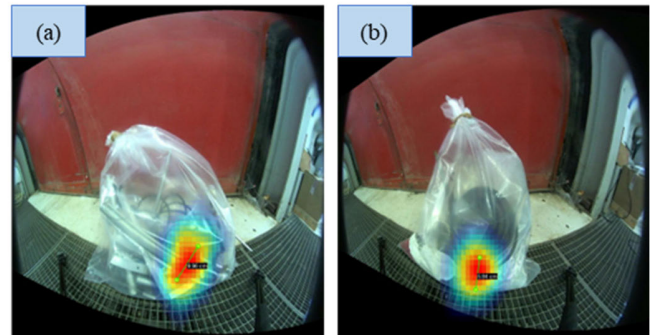

Fig. 6. ^{60}Co image for (a) bag 1 and (b) bag 2. The real time was ≈24 h for both measurements.

and so on), no gamma emitters were revealed. In bags containing metallic waste, ^{60}Co was identified and imaged (see Fig. 6).

From the images, the characteristic length associated with the ^{60}Co distribution was ≈10 and ≈6 cm, respectively, for "bag 1" and "bag 2." These lengths are calculated considering 2 "representative points" and assuming that they are on the same plane parallel to the detector and placed at a distance fixed by the user. The detector calibration and the distance inserted by the user provide the needed degrees of freedom for determining each point position in space and, thus, their distance. This calculation, although not perfect, has a minor uncertainty if compared to the one introduced by the user in selecting the points: at this stage, in fact, the radioactivity distribution is on a 2-D plane, no "depth" is considered, and thus, no correction is applied accounting for different distances and paths in the matrix (i.e., absorption). For this reason, although very useful, the distances measured in this way are typically considered only qualitative for retrieving rough spatial information.

The two radioactive bags were measured using the NGI system and an HPGe-based ISOCS system, in order to quantify the amount of radioactivity and to assess the impact, the image reconstruction can have on the quantified amount. Spectra from the imaging system and HPGe were blindly analyzed to avoid bias, although the imaging reconstruction was used also in the detailed HPGe analysis.

Finally, materials have been removed from the bags and placed in distinguished positions on the floor. They have then been measured by gamma imaging to identify the radioactive items. Three items were identified for the total size of 4 × 13 × 1 cm (to be compared with the characteristic length
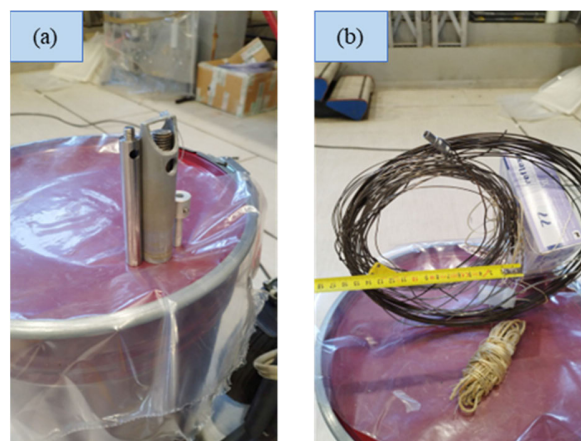
Fig. 7.   Radioactive items contained in (a) bag 1 and (b) bag 2.

estimated by imaging of ≈10 cm) for bag 1, while for bag 2, an activated thermocouple wire has been identified, with the main hotspot having a size of 5 cm (to be compared with the characteristic length of 6 cm estimated by imaging). The items have been measured as "single item" (as they are in Fig. 7) with the HPGe ISOCS system, estimating the most reliable ^{60}Co activity.

Results of all analysis are reported in Tables II and III. The uncertainties provided in the tables are the sum in quadrature of two main sources: counting statistics and efficiency modeling. The first depends upon the spectra (peak size, Compton continuum, and interferences among peaks) and is automatically calculated by the two systems used. The latter is the uncertainty associated with the point-kernel-based algorithm both systems used for efficiency calculation.

The efficiency uncertainty for the ISOCS system is based on the tests performed by the manufacturer for validating the method [27] (reaching ~15%–20% in some cases and even larger at low energy) and for "characterizing" the detector-specific response.

NGI automatically computes the statistical uncertainty regarding calculation method and the efficiency uncertainty due to the simplifications in the calculation method; however, with respect to ISOCS, NGI lacks at the moment an extensive validation campaign assessing its performances and, thus, the overall method uncertainty. However, in past experiments [13], NGI uncertainty has well reproduced the overall system performances, and thus, no other uncertainty source has been included in this work.

The uncertainty due to the assumptions about the efficiency model (i.e., mainly the matrix distribution in the item to assay and the radioactivity distribution in the matrix) is not considered. These distributions can potentially highly impact the efficiency values and, thus, the activity results: their impact strictly depends upon the kind of item to assay, and the energy considered. Nevertheless, practical experiences and intercomparison exercises attended [28], [29] suggest that a ±15%–20% bias (compatible to the ISOCS uncertainties discussed above in the text) when using ISOCS/NGI to assess radioactivity in "standard" objects (e.g., bags and drums) should be expected due to the simplification introduced by the

modeling with respect to the real case analyzed. This means that, at least for such "standard" object, the typical uncertainty is not heavily impacted by the matrix and contamination distributions.

Three different assumptions regarding the efficiency model have been made for analyzing the two bags, corresponding to a different letter in Tables II and III (A, B, or C). In case A, it was assumed that radioactivity was homogeneously dispersed in the entire bag. The bag dimensions are measured, but the detailed mass density is unknown, and thus, an apparent density was used (calculated by dividing the net mass for the bag volume). In case B, the bag is modeled in the same way as case A, but the radioactivity is localized in a volume determined according to the information (i.e., position in the bag and size) obtained from NGI (see Fig. 6).

In case C, the radioactivity items have been removed from the respective bag and measured in the configuration reported in Fig. 7: the matrix model (that was the entire bag in cases A and B) describes only the items, and thus, the mass density is much more realistic. The radioactivity distribution in case C is assumed to be homogeneous in the matrix modeled. Case C being the one with the most "faithful" model used for efficiency calculation (only radioactive items measured) will be considered as representative of the true value (which is unknown) and used as a benchmark for the other cases' results.

For all cases, the uncertainties calculated for ^{60}Co activity determination are coming from counting statistics mainly, while the model-related uncertainty is lower thanks to the model simplicity. Uncertainties are quoted at 2σ. In the calculation of the activity concentration, volumes and masses calculated (case B) or measured (case C) as explained before are used for error propagation.

For bag 1, with respect to the activity determined by the HPGe ISOCS system after the isolation of the items (case C), the NGI-helped ISOCS evaluation (case B) produces a –23% result (^{60}Co activity, ISOCS-Case B versus ISOCS-Case C), while the traditional ISOCS evaluation (case A) produces a +8% result (^{60}Co activity, ISOCS-Case A versus ISOCS-Case C). For bag 2, with respect to the activity determined by the HPGe ISOCS system after the isolation of the items (case C), the NGI-helped ISOCS evaluation (case B) produces a –17% result (^{60}Co activity, ISOCS-Case B versus ISOCS-Case C), while the traditional ISOCS evaluation (case A) produces a +70% result (^{60}Co activity, ISOCS-Case A versus ISOCS-Case C). Considering that in practical ISOCS utilization, a standard ±15%–20% modeling bias has to be expected, the NGI imaging outcomes do not impact the ISOCS evaluation for bag 1, while it could avoid the +70% overestimation for bag 2.

Regarding the NGI quantification results, with respect to the corresponding ISOCS results (case C), it could be noted that NGI activity values are included in a range of −3% to 17% and they are compatible with ±15%–20% bias in ISOCS utilization. NGI and ISOCS results appear to be aligned (comparing case A with respect to case B), within the modeling uncertainties discussed. The NGI detector could be intended, in such a sense, as an alternative solution to

TABLE II
ANALYSIS RESULTS FOR BAG 1

Case	Matrix model	Radioactivity distribution	^{60}Co Activity [kBq]		^{60}Co Activity Concentration [Bq · g^{-1}]	
			NGI	ISOCS	NGI	ISOCS
A	Whole bag, box shape 40 cm × 20 cm × 25 cm, filling matrix: iron at apparent density 0.7 g · cm^{-3}	Uniform in matrix	1.6 ± 0.3	1.68 ± 0.06	0.11 ± 0.02	0.12 ± 0.01
B	Whole bag, box shape 40 cm × 20 cm × 25 cm, filling matrix: iron at apparent density 0.7 g · cm^{-3}	10-cm cube at bottom (gamma imaging supported modelling for ISOCS)	1.0 ± 0.2	1.20 ± 0.05	0.07 ± 0.02	0.09 ± 0.01
C	Isolated items, box shape 4 cm × 13 cm × 1 cm, filling matrix: iron at apparent density 3.84 g · cm^{-3}	Uniform in matrix	-	1.55 ± 0.09	-	7.75 ± 0.45

TABLE III
ANALYSIS RESULTS FOR BAG 2

Case	Matrix model	Radioactivity distribution	^{60}Co Activity [kBq]		^{60}Co Activity Concentration [Bq · g^{-1}]	
			NGI	ISOCS	NGI	ISOCS
A	Whole bag, box shape 30 cm × 30 cm × 30 cm, filling matrix: iron at apparent density 0.74 g · cm^{-3}	Uniform in matrix	9.9 ± 0.5	11.9 ± 0.4	0.50 ± 0.03	0.60 ± 0.02
B	Whole bag, box shape 30 cm × 30 cm × 30 cm, filling matrix: iron at apparent density 0.74 g · cm^{-3}	6-cm cube at bottom (gamma imaging supported modelling for ISOCS)	5.6 ± 0.3	5.8 ± 0.2	0.28 ± 0.02	0.29 ± 0.01
C	Isolated items, disk shape 30 cm in diameter × 1 cm thickness, filling matrix: iron at apparent density 0.7 g · cm^{-3}	Uniform in matrix	-	7.0 ± 0.5	-	14.0 ± 1.0

the traditional HPGe ISOCS system, in some cases producing more accurate results also due to the imaging ability. This means that, whatever HPGe-based gamma spectrometry is used for characterization and classification of radioactive waste (according to [30]), gamma-ray imaging could be used with similar performances.

As can be noted, including information from gamma imaging in the model for the measurement efficiency calculation does not always imply an improvement of gamma-spectrometry accuracy. Gamma imaging is "expected" to make the gamma-spectrometry quantification more accurate because of the higher level of detail introduced in the radioactive distribution model. Nevertheless, reality does not always match expectations, for two main reasons (which can be correlated, amplifying their influence on the measurement). The first is that present gamma imaging results are planar reconstructions, and the 3-D model (i.e., shape, dimensions, and location) of radioactivity must be "guessed" by the user, which can of course commit some mistake.

The second reason is that the matrix distribution in the bag's model is not known in detail: if radioactivity is localized in a high-density item, the item itself is absorbing part of the emission in a way, which is not quantified. Conversely, the radioactivity can be localized in a lower mass density item placed inside a matrix with a higher average mass density.

Looking at the items found to be radioactive in bag 1, the first possibility (radioactivity placed in items with mass density higher than the average mass density of the bag) is realized: the radioactive items have, in fact, an average mass density more than a factor of 5 higher than the mass density averaged on the entire bag. In this case, the quantified activity is expected to be lower than the true activity and including gamma imaging information in the model (case B) can even worsen the accuracy, as effectively shown in Table II. In bag 2, the mass density of radioactivity items is similar to the one of the entire bag, and thus, the main impact is due to the position of the radioactive spot: including information provided by gamma imaging (case B) brings an improvement in results' accuracy.

The most significant improvement that NGI introduced in waste management here has been found as the direct identification of the "active" items that have been isolated from the bulk of other materials for a separated radiological characterization. Gamma imaging has the advantage to combine radiological and visual image information, while HPGe has no such ability. In the last case, to find the "active" item in the bulk, the

operator should separate the supposed item manually and test it separately with the HPGe detector, searching until the "active" object(s) is (are) found. NGI applied to the case here has superseded this approach, saving work time for the "sorting" operator, and reducing both the external irradiation exposure and potential risk contributions in manipulating the bulk of radioactive materials.

The identification of the actually "active" item in the bulk, whatever the method, is another relevant advancement in waste management. As can be seen in Tables II and III, the activity concentration of the isolated items is almost two orders of magnitude greater than homogeneously dispersed activity concentration values. In reactor management, the personnel is not expected to test each item to check its radiological state and sort it accordingly, e.g., the "radioactive bin" or the "potentially radioactive" one. The whole material is considered to be radioactive, and the determined activity is then distributed over the whole matrix. In the NGI activities carried out at the TRIGA RC-1, the experiment showed that the gamma imaging ability could improve the waste management, potentially allowing a sorting capability of certainly radioactive items with respect to other materials, in a way that could be compatible with the reactor day-life routine, i.e., using rest time of the night and weekend to take radiological characterization measurements.

B. Case 2: Analysis of a TRIGA-Type Fuel Element

The fresh fuel storage room was inspected as part of the survey, including the direct measurement of a fuel element placed in a convenient position in the room [13]. The element was used when the TRIGA was run at 100-kW thermal power, and since its upgrade to 1 MW, it has been safely stored in the fresh fuel storage. Its weight is 3.4 kg, and it is made of HZr-U expected to contain 34 g of ^{235}U. Other details about the elements and their assembly are known from the historical knowledge of the TRIGA reactor [31].

The NGI reconstructions are reported in Fig. 8: ^{235}U (key line at 185.7 keV) is imaged in the forward direction at the center of the element in agreement with the reconstruction of low-energy emissions from ^{234}Th (a ^{238}U daughter in secular equilibrium) decay. Differently, high-energy emissions from ^{234m}Pa (another daughter of ^{238}U in secular equilibrium) are reconstructed in the backward direction (the black area in the image represents the rest of the entire solid angle with respect to the optical image since the Compton imaging is possible on almost all possible incoming directions) because of the presence of a large amount of natural uranium elements stored in the immediate surrounding.

The nonuniformity of reconstructions in Fig. 8(a) and (b) is expected to be due to a noncorrected distance effect and to the low-energy gamma-ray self-absorption. The distance between the detector and the fuel element has been accurately measured; however, the fuel element has a vertical distribution and the exact distance between the detector and each single piece of the distribution is changing. Because the detection efficiency decreases as the distance increases, some bias is introduced in the reconstruction, which results in more
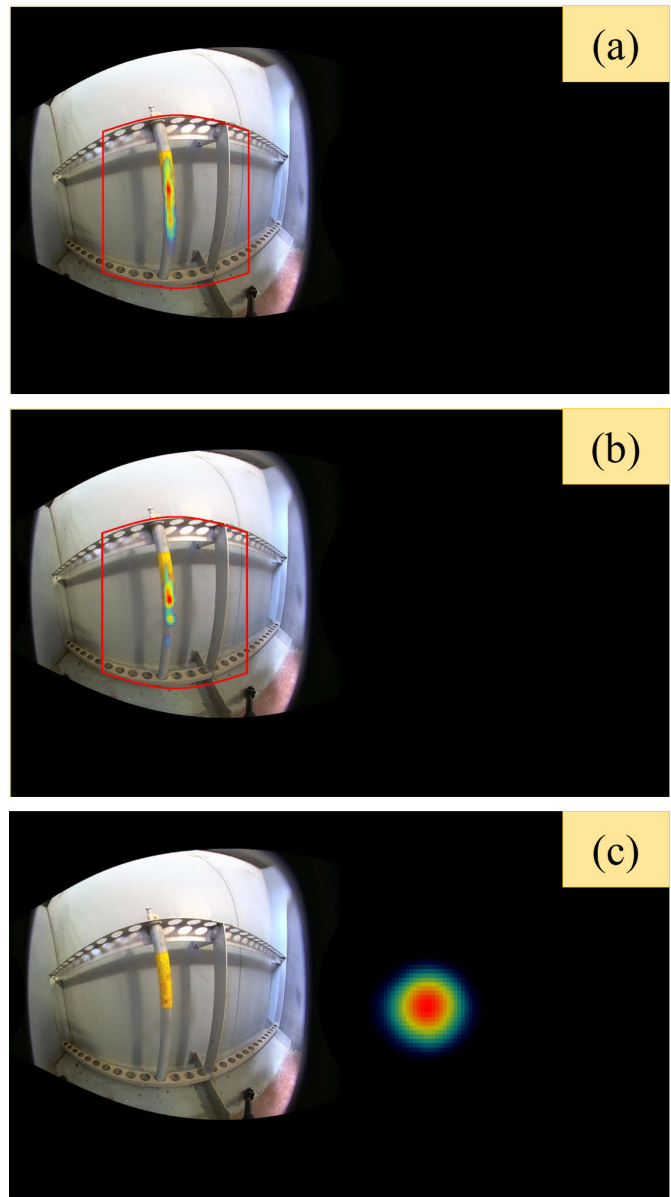

Fig. 8. (a) Image of ^{235}U and ^{238}U (using low- and high-energy lines in (b) and (c), respectively) for a fresh fuel element used in the 100-kW operation phase [14]. The black area in the images represents the complement of the optical image to the entire solid angle. The real time was ≈19 h. Fuel element: (a) ^{235}U (186 + 144 + 163 + 205 keV), (b) ^{234}Th (63 + 92 + 93 keV), and (c) ^{243m}Pa (1001 + 766 keV).

localized toward closer pieces. This effect cannot be accounted for at the moment without further improvements.

A dedicated background measurement was also acquired and used to correct both imaging reconstructions and uranium mass quantification. The background is being strictly dependent upon the detector position, and another fuel element acquisition was taken too. For operative reasons, these acquisitions lasted much less than the first one (around 2 against 19 h), with a consequent lack in statistics power. Despite the short acquisition time, the background subtraction provided some interesting results. Fig. 9 shows the imaging subtraction applied to the energy range 250–1001 keV, corresponding to the main ^{238}U photopeaks (i.e., 1001 and 766 keV from ^{234m}Pa decay) and their Compton continuum (in that range, no other

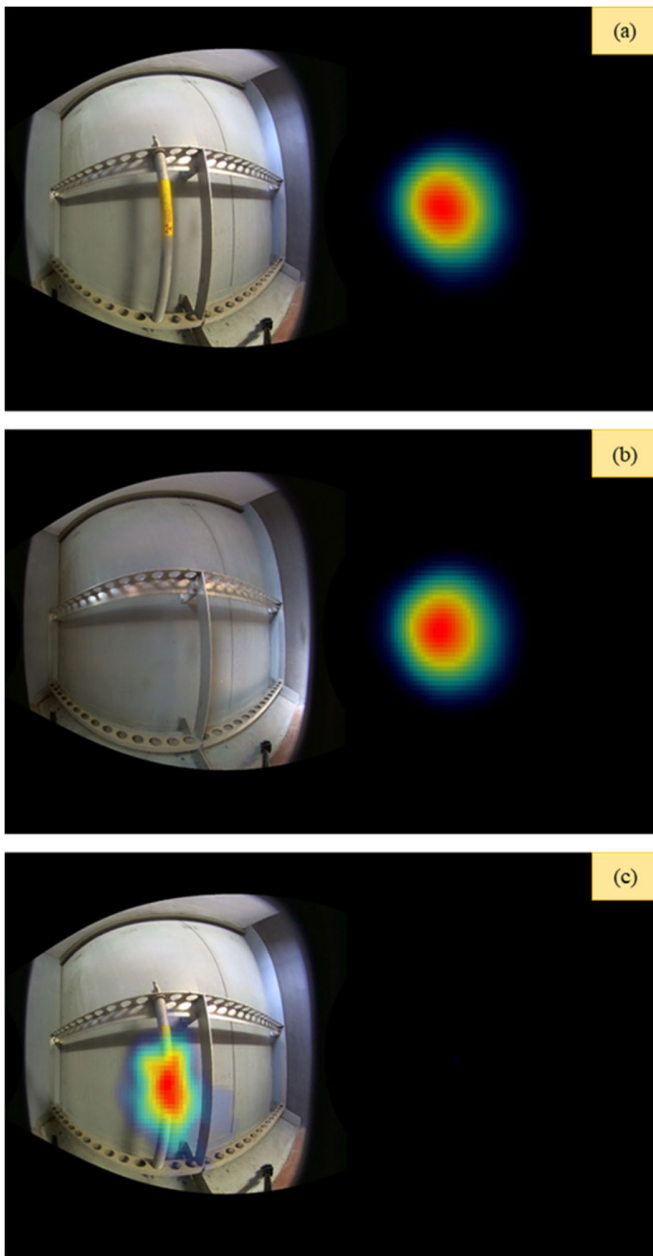Fig. 10. (a) ^{235}U spatial extent as measured by NGI. (b) Size of the entire element as measured by NGI.

Fig. 9. Background subtraction in imaging reconstruction of energy range 250–1001 keV. (a) Fuel element, reconstruction doomed by background. (b) No fuel element, background only. (c) Fuel element after background subtraction. The real-time was ≈2 h for both measurements.

contribution is expected, ^{235}U being the only other measured radionuclide, whose emission with higher energy is 205 keV): including the Compton continuum permits to partially recover the lack in statistics affecting the reconstruction using only photopeaks. Fig. 9 reports the reconstruction of signal from the fuel element plus the background (a), the background only (b), and the net signal from the fuel element: the image of the net signal is localized on the fuel element, although it is noisy because of the subtraction and because it includes the continuum contribution due to the environment.

The characteristic length associated with the ^{235}U distribution (evaluated according to the same method discussed for Fig. 6) is ≈27.8 cm [see Fig. 10(a)], against the value of 38.1 cm known from the element assembly. However,
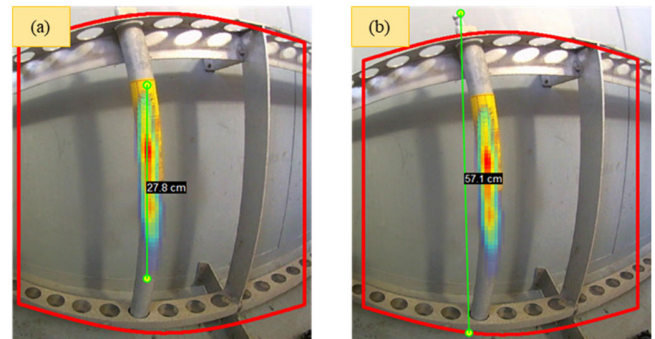
as already said, the parallax correction for length quantification is still to be improved, but differently from the bags, in the fuel element case, the radioactivity distribution can be assumed as monodimensional (only the height). This simplification permits to infer a correction using some known length as a reference, such as the entire element size equal to 72 cm from the fuel assembly drawing. The corresponding value estimated by imaging is 57.1 cm: applying a simple proportional correction, the ^{235}U characteristic length returns to be (27.8 × 72)/57.1 ≈ 35 cm. The residual difference with respect to the real value is expected to be due to the noncorrected distance effect, producing an image less spread than it should be.

Differently, with respect to what was presented in [14], the quantitative analysis has been done on the background-free spectrum, obtaining a mass of ^{235}U of (36.3 ± 1.75) g against the 34 g expected and a mass of ^{238}U of (189 ± 34) g against the 152 g expected. Both values agreed within 1- or 2-sigma uncertainty with the expected masses.

The NGI applied to the TRIGA-type fuel element has shown the capability to characterize the mass of SNMs as well as visualize the distribution of radioactive materials. In the field of nuclear safeguards, in which instrumental detection during inspections is usually relying on qualitative radionuclide spectral identification, i.e., ^{235}U/^{238}U energy lines for nonirradiated items, plus ^{60}Co/^{137}Cs for irradiated items (e.g., identiFINDER [31] or equivalent detectors), the ability to visualize the SNM by human eye and check its stability versus time and previous snapshots taken, could be a valuable advancement of current nonproliferation protocols applied during inspections. Moreover, the gamma imaging data supplied with geometrical information (by LIDAR, mapping engine, and so on) would allow postponed analysis and the possibility of quantitative characterization after the technical inspection also: with the visual image, geometries, distances, and technical information of the item (e.g., technical drawing of the fuel element), the postprocessing of the whole data would lead to quantification of masses of SNM also, potentially increasing robustness in nonproliferation actions.

C. Case 3: d-t Neutron Generator Operation Campaign

In TRIGA RC-1 Reactor Hall, some neutron generator (NG) devices are stored. In particular, a portable Thermo Scientific MP 320 deuterium–tritium 14-MeV NG [33] is used for several irradiation experiences, e.g., irradiation of samples,
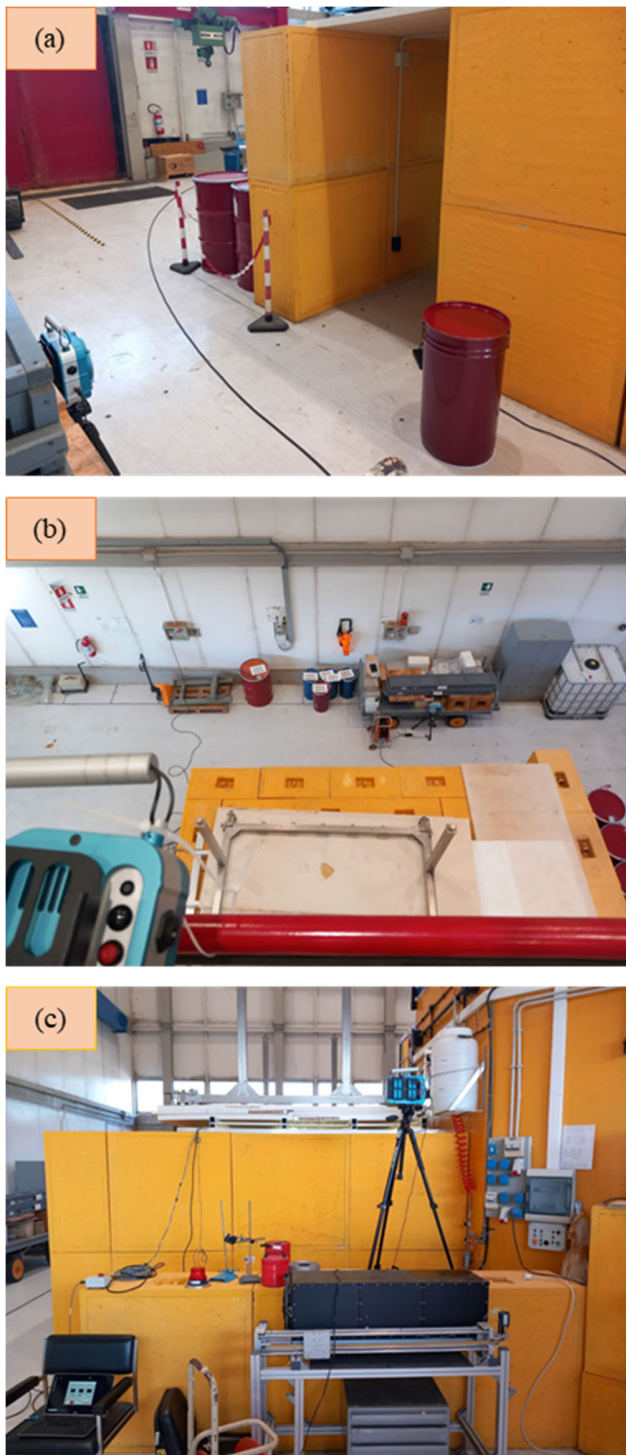
Fig. 11. Setups used for measuring the bunker from (a) entrance, (b) Reactor Top, and (c) one side during neutron irradiation experiment.

Fig. 12. Time spectrum for all gamma rays reaching the detector while and after NG functioning.

to test counting electronics, innovative neutron detectors, or SNM detection systems. The NG is operated at the Reactor Tangential Channel Bunker, i.e., a 1-m shielded room made of concrete blocks at the side, with a 10-cm high-density polyethylene ceiling. The rationale in using the NGI imaging system here is to monitor the streaming effect of gamma radiation escaping the inside of the bunker from the pass labyrinth and the ceiling.

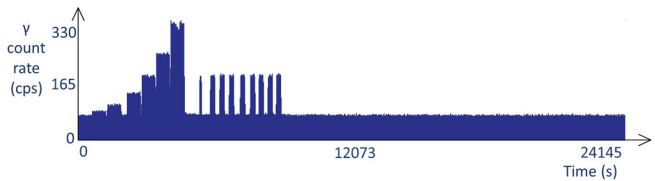During an irradiation campaign using the NG in September 2023, the NGI was used to test the concept. The effect was detected on the gamma flux rate at the detector position; thus, a couple of dedicated measurements were taken around the shielded area where the generator was used. The goal here was to establish the main gamma streaming pathways for radiation protection optimization (i.e., escape path to be shielded to reduce gamma dose rate within the reactor hall). Three different measurement setups were considered: looking at the bunker entrance, looking at the bunker ceiling from the Reactor Top, and looking from one side (see Fig. 11).

The time spectrum (i.e., the gamma count rate versus time) for the measurement taken at the bunker entrance is reported in Fig. 12. In the first part of the measurement, the neutron yield was increased as was the total gamma flux generated by neutron-induced secondary events (a count rate up to $\approx$320 cps was recorded, at incremental steps proportional to the neutron yield, while the environmental count rate was $\approx$70 cps, with the generator off). In the second part, the generator was pulsed repetitively at the same neutron yield and a sort of "comb" in gamma count rate is clearly visible in the time spectrum (at $\approx$170 cps). In the remaining part of the measurement, with the NG off, the gamma count rate remained "flat" at environmental values.

Because of the capability of the NGIs to acquire time spectra, the "environmental" section of the total measurement was used as radiological background, to be subtracted from the "active" section due to the NG operation, to enhance the imaging reconstruction. Low-energy photons (from 250 to 1.5 MeV) and high-energy photons (from 1.5 to 3.0 MeV) were considered separately for all the three positions. The low-energy range contains most of the photopeaks generated in nuclear decays and has a relevant continuum background, overall representing the main contribution to the dose rate after NG functioning. The high-energy range has a lower continuum background and can provide information about processes different than α- and β-decay: examples are the activation peaks (such as 2.2 MeV due to hydrogen in the neutron moderator) or the delayed photon emission due to the (α, n) reaction, such as the Doppler-shifted 4.4-MeV emitted by beryllium in a neutron source such as RaBe or AmBe.

Although small, some photopeaks can be distinguished in spectra acquired (see Fig. 13). In particular, peaks at $\approx$558 and $\approx$651 keV were detected, which are due to interaction in cadmium layers included in the bunker walls. Furthermore, a broad peak is visible in the 474–478-keV range, which is expected to be due to boron neutron capture (the large Doppler shift is due to lithium recoil). Unfortunately, both cadmium and boron are present also in the imaging detectors (cadmium in the crystal and boron in the electric circuits), and the events happening in the detectors are as a background for the imaging
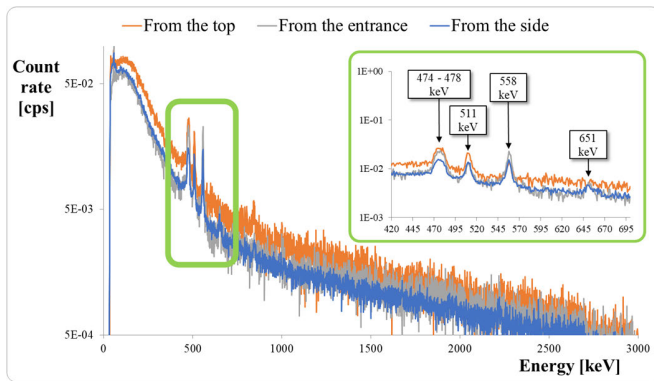
Fig. 13. Background-free energy spectra collected during the irradiation campaign.
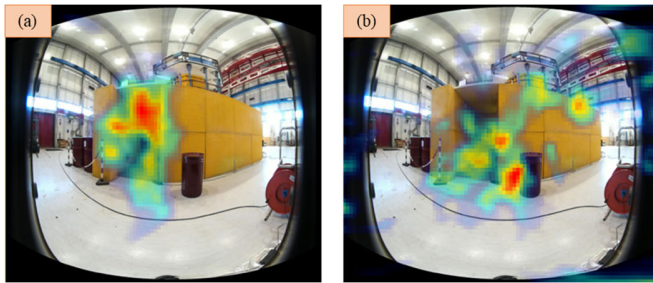

Fig. 15. (a) 250–1500-keV and (b) 1500–3000-keV energy ranges for the measurement taken looking at the ceiling, with the detector placed ≈6 m away from closer scattering materials. The real time was ≈7 h.

Fig. 14. (a) 250–1500-keV and (b) 1500–3000-keV energy ranges for the measurement taken looking at the entrance, with the detector placed ≈2 m away from closer scattering materials. The real time was ≈7 h.

Fig. 16. (a) 250–1500-keV and (b) 1500–3000-keV energy ranges for the measurement taken looking at the side, with the detector placed ≈1 m away from closer scattering materials. The real time was ≈24 h.

of the events happening in the bunker: as a consequence, the imaging of cited peaks does not add relevant information with respect to what is presented further.

For the measurement taken at the entrance (see Fig. 14), both fluxes (low energy and high energy) were generated by scattering and gamma generation happening in the wall and in the portion of the ceiling visible from the entrance; for high-energy photons, thanks to their higher penetration, the probability to pass through the wall is more important, as is the scattering on the floor. For the measurement taken toward the ceiling from the Reactor Top (see Fig. 15), both fluxes were coming from the high-density polyethylene ceiling, although the high-energy flux shows a wider distribution (interactions in the walls) and also a concentration close to the NG itself. For the measurement taken from the side (see Fig. 16), the low-energy flux mainly comes from the polyethylene ceiling, while the high-energy flux has the most important component passing through the wall before reaching the detector.

In all measurements done, a substantial noise is present (in particular for the measurement taken at the entrance, Fig. 14, despite the larger amount of events with respect to the other two measurements as clearly visible from the spectra): it is due to the real distributions being very complex (they are all representing scattering and secondary events happening in walls and floor) and not localized in some "preferred" scattering materials (as can instead be seen in [13, Fig. 8]). Such distributions, to be reconstructed, would require a higher number of events than the number that was possible to record during the irradiation campaign.
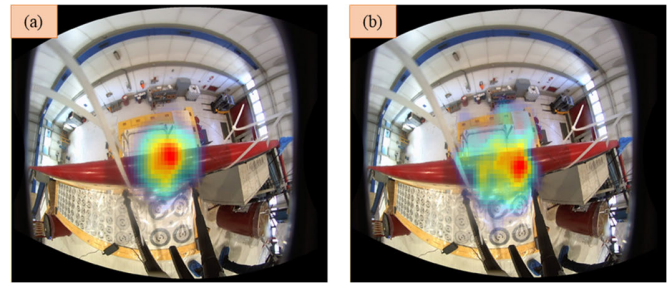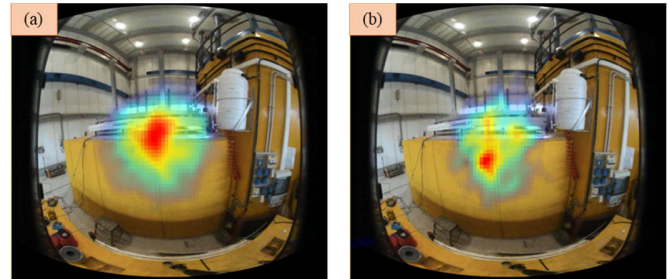
In particular, in measurements from the top and from the side, the polyethylene ceiling is functioning as the main scatterer, i.e., most of the photons detected are coming from it: the distributions are less scattered and thus easier to reconstruct. In the measurement from the entrance, the portion of ceiling "visible" (i.e., from where photons can reach the detector without passing through the wall) is lower, and then, the probability for a photon to reach the detector after having scattered in the wall gets relatively higher with respect to the other two measurements: this means that the overall distribution of detected photons is more scattered and thus more difficult to be reconstructed.

The information collected during the NG irradiation campaign can be used to understand the main directions from which gamma rays are escaping the irradiation area and, thus, the main directions to be shielded to reduce the radiation streaming. In case the streaming path is found to be void, the gamma streaming information is also useful to assess neutron escaping pathways. The conclusion is that gamma imaging applied to the irradiation experiments could be a useful tool to better understand and visualize radiation's physical behavior and to study countermeasures to limit the streaming pathways, optimizing the personnel exposure.

The same concept will be applied to reactor irradiation channels also, in a future activity that is expected to redesign and refurbish them for newer applications and experiments.

The pulsed operation of the NG, clearly visible in the bunches of bursts of gammas detected versus time in Fig. 12, is particularly useful to discuss the added capability that the NGIs have to manage the "time variable." Gamma events detected in the crystal are recorded each one with a specific time tag: this information allows to "roll out and back" the

acquired measurement as desired, in sectioning, analyzing, and producing results taking the "time variable" in account also.

Although HPGe manufacturers can introduce this time "resolution" capability in their detectors with a relatively little effort, it is not generally provided, and thus, only time-cumulated spectra are produced. One of the reasons behind that is that the time information in HPGe can be used (at least as main application) for trend analysis (i.e., looking at the trend in activity of a certain radionuclide in a precise part of a system or component): in any other application, a detected time variation would lack the possible explanation about what could cause it and thus often the entire measurement may be susceptible to be rejected. On the contrary, coupling the timing information to optical and radiological imaging can permit to correlate variation in the trend to its possible cause (e.g., a radioactive material transported in the surrounding of the detector in a short timeframe during a long acquisition) and then analyze the measurement in different time bins (even coupling nonconsecutive time bins while excluding other or treating them as background).

D. Case 4: Assay of a Bunker Content

Within the TRIGA RC-1 Reactor Hall, the radioactive sources and the more radioactive materials are stored in a specific area called "the Bunker." This structure has concrete walls and no ceiling, allowing to move items in and out by means of the Reactor Hall crane. Several NGI acquisitions have been taken from different sides and positions and looking inside the bunker from the top [14].

Fig. 17 reports some of the setups used and the main results. The presence of one ^{226}Ra and two ^{241}Am hotspots can be distinguished. Furthermore, a higher photon yield in the energy region from 1.7 to 3 MeV is detected (probably dominated by the Compton continuum due to the 4.4-MeV delayed gammas emitted after beryllium transmutation), as long as the 2.2-MeV photon characteristic of (n, γ) reaction on hydrogen (deeply used for shielding of neutron sources, e.g., paraffin or polyethylene): both these ranges images are spatially matching the reconstruction of ^{226}Ra and ^{241}Am, thus strongly suggesting the fact that the sources are actually RaBe and AmBe neutron sources, which is in agreement with the radiological inventory of the installation. Moreover, the reconstruction of 2.2-MeV line is actually bigger, suggesting the presence of more neutron shielding in the area (and so possibly another low-activity or highly shielded neutron source). Finally, ^{137}Cs is imaged as widely spread over components present in the bunker, while ^{60}Co reconstruction is dominated by a single activated item (the photon yield is high enough to permit the reconstruction using the coded aperture mask for such high energy).

The bunker reserved other two "lessons learned" while pursuing the goal of surveying in its surrounding. The first (see Fig. 18) was the capability to detect a small ^{60}Co signal (turned out to come from a source stored in a small shield) in a reconstruction dominated by the signal coming from the activated item already discussed and reported in Fig. 17.
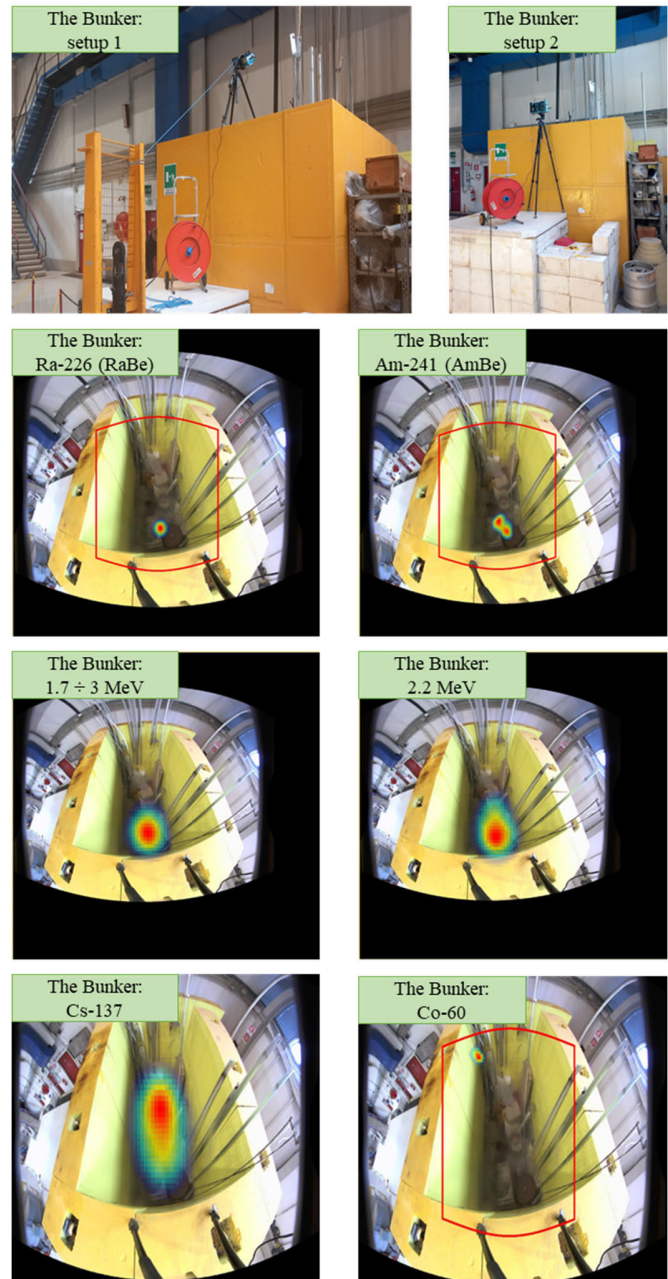

Fig. 17. Detected radionuclides inside the bunker area [14].

The second was the detection of a steady signal coming from a large polyethylene shielding (measurement done in setup 2 of Fig. 17). Three clues suggest that this signal is coming from an AmBe neutron source (see Fig. 19): the presence of the 2.2-MeV peak characteristic of the (n, γ) reaction on hydrogen (i.e., a neutron source interacting in polyethylene) and a large count rate in the high-energy range (due to the continuum of 4.4-MeV delayed photons), both being reconstructed in the same position (corresponding to the polyethylene shield), and the absence of any other identified gamma peak (a significant ^{226}Ra activity would be easily detectable, and thus, the alpha emitter is expected to be ^{241}Am according to the installation inventory).
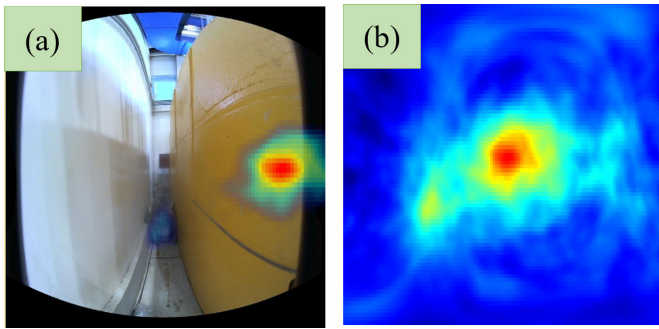
Fig. 18.   Detection of a small ^{60}Co source placed in a shield outside the bunker area as a tailing effect (a) of the main reconstruction dominated by the activated component [14]. The tail is more evident if the optical image is removed (b).
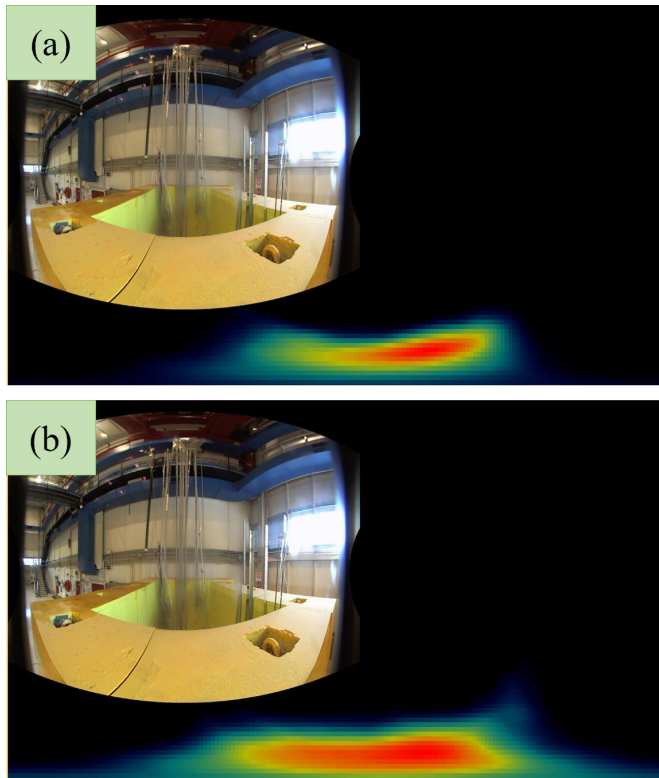

Fig. 19.   Imaging reconstruction of the 2.2-MeV peak due to interaction of neutrons with hydrogen (a), and of all gamma rays in the range from 1.7 MeV to 3 MeV (b), suggesting the presence of a AmBe neutron source at the external side of the Bunker [14].

IV. Conclusion

A state-of-the-art gamma-ray imaging and spectrometer has been extensively tested at the TRIGA RC-1 Research Reactor at the ENEA Casaccia Research Center to evaluate its capabilities in a wide range of applications. The experience has demonstrated that the technology is suitable for survey tasks, in particular identifying hotspots, unknown radioactive items, loss of containment, and localizing sources. With some care taken, signals and images triangulation can allow the localization of unexpected radioactive spots or items, as well as the sorting of certain radioactive items from potentially nonradioactive items.

The capability to visualize the radioactivity, and to provide information about its spatial distribution in a generic item, can also improve accuracy in quantification of other nondestructive

characterization techniques, namely, HPGe gamma spectrometry: as shown, the presence of small radioactive hotspots in larger items can heavily impact gamma-spectrometry characterization results. Knowing dimensions and position of those hotspots thanks to gamma-ray imaging can allow a more accurate estimation of radioactivity content, often avoiding possible severe underestimation/overestimation (such as presented also in this work) with respect to the overall bias of $\approx$15%–20% for mid-/high-energy emissions typically considered when using this kind of techniques.

Even better, gamma-ray imaging can avoid mixing radioactive and nonradioactive items, further improving accuracy in activity concentration characterization, and also reducing the overall amount of radioactive waste with a better classification of materials.

The imaging system used has proven a quantification capability of gamma-emitting content at the same level of other worldwide accepted gamma-spectrometry systems. This capability, coupled with the radioactivity distribution information natively provided by the imaging technique, can make this kind of system a (more than) serious alternative option when quantification is required. This quantification capability has worked also in a complex case like a fuel element for uranium quantification, returning values in agreement with the expectation within uncertainties at the same level of HPGe-based gamma spectrometry.

Imaging and quantification capabilities, together with the possibility to analyze the time spectrum, make this sort of system interesting for safeguards and nonproliferation activities, such as a monitoring system to prevent diversion of nuclear material and to ensure the CoK.

Finally, during installation operations, such as the case tested of a pulsed NG in use, the gamma-ray imaging technique can help determine the main irradiation channels, i.e., the direction gamma rays are coming from considering a certain position. This kind of information, together with time spectrum analysis, can permit to understand where possible additional shielding may be employed to reduce personnel exposure or in case a loss in containment or shielding may happen, thus improving the continuity of radiation protection for operators.

Research is still ongoing to further improve imaging technology. Nucleco is currently validating new hardware (LIDAR, odometry camera, and on-board robotic system) and software (mapping engine, such as Google Carthographer [34]) add-on to fill some gaps that the current 2-D imaging system has, creating a proper simultaneous localization and mapping (SLAM) system aware of the space all around it (such as in [35]). This SLAM-based system will be capable to determine at each timeframe the detector's position and pose (i.e., rotation angle with respect to the three Cartesian axes) in space and to figure out the space in the format of a point cloud. This will provide the imaging system the spatial awareness needed for projecting 2-D reconstructions in 3-D space. The result is the 3-D distance-corrected radioactivity reconstruction inside a "measurable" space (the point cloud provides the spatial information to measure distances), which can leverage the gamma-spectrometry efficiency modeling (whose calculation

can then account for varying distance) and the knowledge of the radiological state of a generic area or component.

REFERENCES

[1] S. Hussain et al., "Modern diagnostic imaging technique applications and risk factors in the medical field: A review," *BioMed Res. Int.*, vol. 2022, pp. 1–19, Jun. 2022, doi: 10.1155/2022/5164970.

[2] Z. T. Al-Sharify, T. A. Al-Sharify, N. T. Al-Sharify, and H. Y. Naser, "A critical review on medical imaging techniques (CT and PET scans) in the medical field," *IOP Conf. Ser., Mater. Sci. Eng.*, vol. 870, no. 1, Jun. 2020, Art. no. 012043, doi: 10.1088/1757-899x/870/1/012043.

[3] Y. Jin et al., "Experimental evaluation of a prototype combined PET-Compton imaging system based on 3-D position-sensitive CZT detectors for dedicated breast cancer imaging," *J. Nucl. Med.*, vol. 62, no. 1, p. 1129, May 2021.

[4] C. G. Wahl et al., "The polaris-H imaging spectrometer," *Nucl. Instrum. Methods Phys. Res. A, Accel. Spectrom. Detect. Assoc. Equip.*, vol. 784, pp. 377–381, Jun. 2015.

[5] H3D. (Dec. 2023). *H420 Gamma-Ray Imaging Spectrometer*. [Online]. Available: https://h3dgamma.com/H420Specs.pdf

[6] E. Jablonowski, M. Kiser, D. Longford, and J. Mitchell, "Application of the PHDS germanium gamma-ray imager (GeGI) in facility decontamination assessment," presented at the WM Symposia Conf., 2019.

[7] G. Montémont et al., "NuVISION: A portable multimode gamma camera based on HiSPECT imaging module," in *Proc. IEEE Nucl. Sci. Symp. Med. Imag. Conf. (NSS/MIC)*, Atlanta, GA, USA, Oct. 2017, pp. 1–3, doi: 10.1109/NSSMIC.2017.8532713.

[8] K. Amgarou et al., "A comprehensive experimental characterization of the iPIX gamma imager," *J. Instrum.*, vol. 11, no. 8, Aug. 2016, Art. no. P08012, doi: 10.1088/1748-0221/11/08/p08012.

[9] J. Hilsabeck, "3D gamma source mapping and intervention analysis," presented at the WM Symposia Conf., 2019.

[10] S. R. Gottesman and E. E. Fenimore, "New family of binary arrays for coded aperture imaging," *Appl. Opt.*, vol. 28, no. 20, pp. 4344–4352, Oct. 1989.

[11] M. Z. Hmissi et al., "First images from a CeBr$_3$/LYSO:Ce temporal imaging portable Compton camera at 1.3 MeV," in *Proc. IEEE Nucl. Sci. Symp. Med. Imag. Conf. (NSS/MIC)*, Sydney, NSW, Australia, Nov. 2018, pp. 1–3, doi: 10.1109/NSSMIC.2018.8824429.

[12] H. S. Lee, J. H. Kim, J. Lee, and C. H. Kim, "Development and performance evaluation of large-area hybrid gamma imager (LAHGI)," *Nucl. Eng. Technol.*, vol. 53, no. 8, pp. 2640–2645, Feb. 2021, doi: 10.1016/j.net.2021.01.036.

[13] F. Gagliardi, D. I. Goodman, E. Gorello, W. Kaye, E. Mauro, and M. Pagliuca, "Reliability of 3D pixelated CdZnTe system in the quantitative assay of radioactive waste: A demonstration," in *Proc. IEEE Nucl. Sci. Symp. Med. Imag. Conf. (NSS/MIC)*, Italy, 2022, pp. 1–4, doi: 10.1109/NSS/MIC44845.2022.10399167.

[14] F. Gagliardi et al., "Seeing radioactivity: Gamma-ray imaging technique applied to TRIGA RC-1 research reactor in ENEA Casaccia," in *Proc. EPJ Web Conf.*, vol. 288, 2023, p. 7013, doi: 10.1051/epj-conf/202328807013.

[15] D. Xu, Z. He, C. E. Lehner, and F. Zhang, "4-pi Compton imaging with single 3D position-sensitive CdZnTe detector," *Proc. SPIE*, vol. 5540, pp. 144–155, Oct. 2004, doi: 10.1117/12.563905.

[16] R. K. Parajuli, M. Sakai, R. Parajuli, and M. Tashiro, "Development and applications of Compton camera—A review," *Sensors*, vol. 22, no. 19, p. 7374, Sep. 2022, doi: 10.3390/s22197374.

[17] T. M. Cannon and E. E. Fenimore, "Coded aperture imaging: Many holes make light work," *Opt. Eng.*, vol. 19, no. 3, Jun. 1980, Art. no. 193283, doi: 10.1117/12.7972511.

[18] T. Meißner, V. Rozhkov, J. Hesser, W. Nahm, and N. Loew, "Quantitative comparison of planar coded aperture imaging reconstruction methods," *J. Instrum.*, vol. 18, no. 1, Jan. 2023, Art. no. P01006, doi: 10.1088/1748-0221/18/01/p01006.

[19] K. P. Ziock et al. (2023). *Efficiency Calibration of the H3D H420 Gamma-Ray Imager*. [Online]. Available: https://www.osti.gov/servlets/purl/1999053

[20] E. W. Weisstein. *Azimuthal Equidistant Projection*. From MathWorld—A Wolfram Web Resource. Accessed: Sep. 2023. [Online]. Available: https://mathworld.wolfram.com/AzimuthalEquidistantProjection.html

[21] H3D. (2023). *Visualizer With SourceTerm*. Accessed: Sep. 2023. [Online]. Available: https://h3dgamma.com/sourceTermSpecs.pdf

[22] I. M. Prokopets, S. I. Prokopets, M. A. Khazhmuradov, E. V. Rudychev, and D. V. Fedorchenko, "Point-kernel method for radiation fields simulation," *Voprosy Atomnoj Nauki Tekhniki*, vol. 5, no. 48, pp. 106–109, 2007.

[23] *Mirion Technologies*. Accessed: Sep. 2023. [Online]. Available: https://www.mirion.com/products/technologies/spectroscopy-cscientific-analysis/gamma-spectroscopy/gamma-spectroscopy-software/lab-applications/s573-isocs-calibration-software

[24] R. Venkataraman, F. Bronson, V. Abashkevich, B. M. Young, and M. Field, "Validation of in situ object counting system (ISOCS) mathematical efficiency calibration software," *Nucl. Instrum. Methods Phys. Res. A, Accel. Spectrom. Detect. Assoc. Equip.*, vol. 422, nos. 1–3, pp. 450–454, Feb. 1999.

[25] *History, Development and Future of TRIGA Research Reactors*, Int. At. Energy Agency, Vienna, Austria, 2016.

[26] International Atomic Energy Agency, Education & Training database on Nuclear Safey and Security. *TRIGA Reactor Characteristics*. Accessed: Dec. 2023. [Online]. Available: https://ansn.iaea.org/Common/documents/Training/TRIGA%20Reactors%20(Safety%20and%20Technology)/intro/start_tmtrr.htm

[27] *Model S573/S574 ISOCS/LabSOCS Validation and Verification Manual*, Canberra Ind., Inc., Meriden, CT, USA, 2002.

[28] E. van Es, B. Russel, and S. Collins, "NPL nuclear industry proficiency test exercise 2019," Nat. Phys. Lab. (NPL), Teddington, U.K., Tech. Rep. NPL REPORT IR 60, 2019, doi: 10.47120/npl.IR60.

[29] E. van Es and A. K. Pearce, "NPL nuclear industry proficiency test exercise 2021," Nat. Phys. Lab. (NPL), Teddington, U.K., Tech. Rep., 2021.

[30] *Classification of Radioactive Waste*, Int. At. Energy Agency, Vienna, Austria, 2009.

[31] L. Di Palo et al., "Progetto definitivo E rapporto di sicurezza del reattore TRIGA RC-1 1 MW C.R. ENEA Casaccia," ENEA, Italian Nat. Agency New Technol., Energy Sustain. Econ. Develop., Casaccia Res. Center, Rome, Italy, Tech. Rep., 1966.

[32] *Teledyne Flir*. Accessed: Sep. 2023. [Online]. Available: https://www.flir.it/products/identifinderr400/?vertical=radiation&segment=detection

[33] *ThermoFisher*. Accessed: Sep. 2023. [Online]. Available: https://www.thermofisher.com/order/catalog/product/1517021A

[34] W. Hess, D. Kohler, H. Rapp, and D. Andor, "Real-time loop closure in 2D LiDAR SLAM," in *Proc. IEEE Int. Conf. Robot. Autom. (ICRA)*, May 2016, pp. 1271–1278.

[35] J. Hecla et al., "Polaris-LAMP: Multi-modal 3-D image reconstruction with a commercial gamma-ray imager," *IEEE Trans. Nucl. Sci.*, vol. 68, no. 10, pp. 2539–2549, Oct. 2021, doi: 10.1109/TNS.2021.3110162.